Volume 1 | Number 1 | Jan 2013 | Pages 1–100

Catalysis Science & Technology

www.rsc.org/catalysis

ROYAL SOCIETY OF CHEMISTRY

This is an *Accepted Manuscript*, which has been through the Royal Society of Chemistry peer review process and has been accepted for publication.

Accepted Manuscripts are published online shortly after acceptance, before technical editing, formatting and proof reading. Using this free service, authors can make their results available to the community, in citable form, before we publish the edited article. We will replace this *Accepted Manuscript* with the edited and formatted *Advance Article* as soon as it is available.

You can find more information about *Accepted Manuscripts* in the **Information for Authors**.

Please note that technical editing may introduce minor changes to the text and/or graphics, which may alter content. The journal's standard **Terms & Conditions** and the **Ethical guidelines** still apply. In no event shall the Royal Society of Chemistry be held responsible for any errors or omissions in this *Accepted Manuscript* or any consequences arising from the use of any information it contains.

Catalysis Science & Technology

Dynamic Article Links ▶

ARTICLE TYPE

Effects of MoO₃ crystalline structure of MoO₃-SnO₂ catalysts on selective oxidation of glycol dimethyl ether to 1, 2-propandiol

Zhenzhou Zhang,[a,b] **Qingde Zhang,**[a*] **Lingyu Jia,**[a,b] **Wenfeng Wang,**[a,b] **He Xiao,**[a,b] **Yizhuo Han,**[a] **Noritatsu Tsubaki**[a,c] **and Yisheng Tan**[a]*

To improve the selectivity of 1, 2-propandiol (PDO) by modifying the structure and morphology of MoO₃/SnO₂ catalyst, orthorhombic (α), monoclinic (β) and hexagonal (h) MoO₃ crystalline phases were prepared to meet the rational design requirements of MoO₃-SnO₂ structure beneficial for the reaction of
10 glycol dimethyl ether (DMET) to PDO. With the increasing reaction temperature, the highest PDO selectivity of the oxidation reaction of glycol dimethyl ether to 1, 2-propandiol was always obtained over h-MoO₃-SnO₂ catalyst and the lowest PDO selectivity was always obtained over β-MoO₃-SnO₂ catalyst, MoO₃ bulk structure, the interaction between SnO₂ and MoO₃ and surface property of these three catalysts could account for this distinctive difference. Hexagonal MoO₃ is dispersed more homogeneously
15 over h-MoO₃-SnO₂ catalyst due to the hexagonal crystalline tunnel structure existing in h-MoO₃-SnO₂ catalyst and the weak interaction between MoO₃ and SnO₂, besides, more hydrated surface of h-MoO₃-SnO₂ catalyst can lead to more Bronsted acid sites on the catalyst surface and favor the dissociation of C-O bond in DMET and association of C-C bond to form PDO with assistance of redox and base sites, which can explain why the highest PDO was obtained over h-MoO₃-SnO₂ catalyst. The lattice strain and
20 oxygen vacancies in β-MoO₃-SnO₂ catalyst induced by the substitution of Sn^{4+} ion with smaller sized Mo^{6+} ion enhance the oxidation ability of β-MoO₃-SnO₂ catalyst, consequently more CH₃O· can be formed and transformed to formaldehyde (FA) and methyl formate (MF), which can explain why the total selectivity of FA and MF was highest while the selectivity of PDO was lowest over β-MoO₃-SnO₂ catalyst at the same time. These findings are pretty significant for further investigation of rational design
25 of MoO₃-SnO₂ catalyst structure applied for the reaction of DMET to PDO.

1. Introduction

In the last decade, conversion of sustainable and environmentally friendly dimethyl ether (DME) to chemicals and fuels has gained increasing attention due to the worldwide energy and
30 environmental problems. In this respect, DME-derived formaldehyde[1, 2] (FA), methyl formate[3, 4] (MF), ethanol[5], dimethoxy methane[6] (DMM), and dimethoxy dimethyl ether[7] (DMM₂), dimethoxyethane[8] (DMET) have emerged as promising chemical products. Herein, we explore the selective oxidation
35 reaction of DMET to 1, 2-propandiol (PDO). PDO is an important chemical as biodegradable functional fluid such as antifreeze, aircraft deicer and lubricant, and as precursor in the synthesis of unsaturated polyester resins and pharmaceuticals[9-14]. However, it is industrially produced by multi-step
40 transformations of non-renewable petroleum-derived propylene[15] currently.

Up to now, Cu-based catalysts have been mainly used to explore the conversion of glycerol to PDO. For instance, $Cu_{0.4}/Zn_{5.6-x}Mg_xAl_2O_{8.6}$ and core-shell Fe₂O₃@CuMgAl
45 catalysts[16, 17] have been investigated and conclusion was drawn that the conversion of glycerol to PDO strongly depended on the basicity of the Cu-based catalysts. Cu/SiO₂ catalysts[18, 19] have been utilized and proposal was made that the dispersion of copper particles and the structure of catalysts affected the PDO
50 selectivity. Besides, Ru/C in the presence of WO₃[20] has been reported as an efficient catalyst for conversion of cellulose into PDO and suggestion was made that fine design of WO₃ structures was significant in the selective cleavage of the C-C bond. Obviously, these studies still come across high reaction
55 temperatures, high H₂ pressures and the use of noble metal Ru. However, fundamental understandings from these reports on the catalyst structural design for PDO and reaction mechanism give us insight into exploring new catalysts to synthesize PDO from other chemical materials.

This journal is © The Royal Society of Chemistry [2015]

[Catal. Sci. Technol.], [2015], **[vol]**, 00–00 | 1

Previously, we discovered that MoO_3/SnO_2 catalyst exhibited catalytic ability in conversion of DMET into PDO. Herein, we aim to modify the structure and morphology of MoO_3/SnO_2 catalyst to improve the selectivity of PDO and simultaneously explore the effects of MoO_3 bulk structure, the interaction between SnO_2 and MoO_3, surface property and the morphology and microstructure on DMET dissociation, intermediate group transformation and PDO formation. C-O bond can be dissociated over acid sites existing on the surface of the catalyst[1], C-C bond can be connected over base sites with the assistance of the redox sites[21], therefore the rational design of MoO_3/SnO_2 catalyst structure needs to strengthen the acid sites, redox sites and moderate the base sites existing on the surface of the MoO_3/SnO_2 catalyst. Hence, the preparation of MoO_3/SnO_2 catalysts was improved, hexagonal (h), monoclinic (β) and orthorhombic (α) MoO_3 crystalline phases were prepared to explore the rational design requirements of MoO_3-SnO_2 structure beneficial for the reaction of DMET to PDO.

In this report, with the increasing reaction temperature, the highest PDO selectivity of the oxidation reaction of glycol dimethyl ether to 1, 2-propandiol was always obtained over h-MoO_3-SnO_2 catalyst and the lowest PDO selectivity was always obtained over β-MoO_3-SnO_2 catalyst. Because of the hexagonal crystalline tunnel structure existing in h-MoO_3-SnO_2 catalyst and the weak interaction between MoO_3 and SnO_2, hexagonal MoO_3 is dispersed more homogeneously over h-MoO_3-SnO_2 catalyst, besides, more hydrated surface of h-MoO_3-SnO_2 catalyst can lead to more Bronsted acid sites in favour of the dissociation of C-O bond in DMET and association of C-C bond to form PDO with assistance of redox and base sites, which can explain why the highest PDO was obtained over h-MoO_3-SnO_2 catalyst. The lattice strain and oxygen vacancies in β-MoO_3-SnO_2 catalyst induced by the substitution of Sn^{4+} ion with smaller sized Mo^{6+} ion enhance the oxidation ability of β-MoO_3-SnO_2 catalyst, consequently more $CH_3O\cdot$ can be formed and transformed to FA and MF, which can explain why the total selectivity of FA and MF was highest while the selectivity of PDO was lowest over β-MoO_3-SnO_2 catalyst at the same time. These findings are pretty significant for further investigation of rational design of MoO_3-SnO_2 catalyst structure applied for the reaction of DMET to PDO.

2. Experimental

2.1 Catalyst preparation

The MoO_3-SnO_2 catalysts with α-MoO_3 and h-MoO_3 crystalline phase were prepared by co-precipitation method. $Na_2SnO_3\cdot3H_2O$ and $(NH_3)_6Mo_7O_{24}\cdot4H_2O$ with the Mo/Sn mole ratio of 2:1 were dissolved into distilled water with stirring, then concentrated HNO_3 three times as many as the mole of $Na_2SnO_3\cdot3H_2O$ was added, heated to 333 K, stirred for 1 h, filtered and centrifuged. The precipitate was dried at 333 K for 8 h under vacuum, then calcined at 523 K for 5 h to obtain h-MoO_3-SnO_2 and calcined at 573 K for 5 h and at 773 K for 8 h to obtain α-MoO_3-SnO_2, respectively.

$(NH_3)_6Mo_7O_{24}\cdot4H_2O$ was calcined at 573 K for 5 h and at 773 K for 8 h to obtain α-MoO_3. $Na_2SnO_3\cdot3H_2O$ and α-MoO_3 with the Mo/Sn mole ratio of 2:1 were dissolved into distilled water with stirring, then concentrated HNO_3 with the HNO_3/Sn mole ratio of

1.76:1 was added, heated to 353 K, stirred for 40 min ,filtered and centrifuged. The precipitate was dried at 373 K for 12 h, calcined at 573 K for 1 h to obtain β-MoO_3-SnO_2.

2.2. Catalytic oxidation of glycol dimethyl ether

The catalytic oxidation reactions were carried out in a continuous flow type fixed-bed reactor containing 2 ml catalysts (20-40 mesh) diluted with 2 ml ground quartz granules (20-40 mesh). The catalysts were pretreated with a flow of O_2 (20 ml/min) for 1 h before reaction at 523 K. The reactant mixture consisted of DMET and O_2 with a DMET/O_2 molar ratio of 1:2. The reaction products were analyzed on gas chromatograph (GC-2014CPF/SPL, Shimadzu) equipped with a FID and a DB-1 column 60 m×0.25 mm and a GC-4000A with TCD (Porapak T column), and on a GC-4000A equipped with a TCD (TDX-01 column) for analyzing H_2, CO, CO_2 and CH_4.

2.3 Catalyst characterization

XRD patterns were measured on a RigakuMiniFlex II X-ray diffractometer, operating at 30 kV and 15 mA and using Cu Kα radiation (λ=0.15418 nm) and a scanning range of 2θ from 5.0 to 70.0°.

IR spectra were recorded by a Bruker Tensor 27 with a MCT detector (64 scans, 4 cm^{-1}), the catalysts were placed in an in situ IR cell equipped with KBr windows (Harrick). For NH_3-IR spectra, the catalysts were heated at 523 K for 1 h under Ar flow, cooled down to 423 K, then NH_3 was introduced, after purging for 30 min with Ar, the spectra were recorded.

The NH_3-TPD profiles were recorded in a fixed-bed reactor system connected with a TCD. The α-, β- and h-MoO_3-SnO_2 catalysts (200 mg) were pretreated at 773, 573 and 523 K under N_2 flow (40 ml/min) for 1 h, respectively, cooled down to 373 K under N_2 flow. Then NH_3 was introduced into the flow system. The TPD profiles were recorded at a temperature rising rate of 10 K /min from 373 to 773 K.

Surface areas of samples were achieved by BET nitrogen desorption isotherms at 77 K measured by TriStarⅡ 3020, pore volume was figured out by t-plot method and pore size was estimated by BJH method on the desorption branch.

XPS were measured on a XPS-AXIS Ultra of Kratos Co. by using Mg Ka radiation (hv=1253.6 eV) with X-ray power of 225 W (15 kV, 15 Ma).

Raman spectra were recorded on a Jobin-YvonLabram-HR Confocal Laser Micro Raman spectrometer with an argon-ion laser at the excitation wavelength of 514.5 nm and the resolution factor of 1 cm^{-1}. The Raman spectra were obtained in the range of 100-1100 cm^{-1} under ambient conditions.

HRTEM images of the catalyst samples were taken with a High Resolution Transmission Electron Microscope (JEM-2010).

SEM images of the catalyst samples were taken with a scanning electronic microscope (JSM-7001F).

3. Results and discussion.

3.1 Effects of α-, β- and h-MoO_3-SnO_2 catalyst on PDO selectivity at different reaction temperature.

Table.1 and Fig.1 present the results of DMET catalytic oxidation and the effects of α-, β- and h-MoO_3-SnO_2 catalysts on PDO selectivity at different reaction temperature, respectively. For all

Table 1 Catalytic oxidation of DMET over α-, β- and h-MoO$_3$-SnO$_2$ catalysts

Cat	T.(K)	DMET Con.(%)	Sel.(C-mol%)					
			CH$_3$OH	FA	MF	MEO	PDO	C$_5$
α	403	4.71	15.6	8.1	26.9	17.3	26.6	5.5
	413	5.64	18.1	9.1	25.4	11.3	31.3	4.8
	423	6.17	20.6	13.7	20.1	10.0	30.8	4.8
	433	7.76	25.2	9.4	29.4	6.2	25.4	4.4
	443	11.95	28.1	8.9	37.3	2.8	20.1	2.8
β	403	5.37	13.3	12.2	32.6	11.0	24.0	6.9
	413	6.12	14.2	10.0	34.8	8.5	27.5	5.0
	423	8.48	15.4	8.5	45.2	5.1	21.6	4.2
	433	9.59	19.0	8.0	42.7	5.2	21.2	3.9
	443	11.65	28.1	7.8	38.9	6.4	17.9	0.9
h	403	4.35	19.3	4.4	20.0	13.4	33.5	9.4
	413	5.24	18.1	4.8	22.6	10.0	38.3	6.2
	423	6.96	19.1	7.7	27.6	8.8	33.2	3.6
	433	9.76	18.9	13.1	27.8	8.2	28.8	3.2
	443	11.62	18.6	17.2	25.9	7.7	27.8	2.8

Reaction conditions: MoO$_3$/SnO$_2$=2:1, DMET/O$_2$=1:2, GHSV=844 h^{-1}
MEO: CH$_3$OCH$_2$CHO
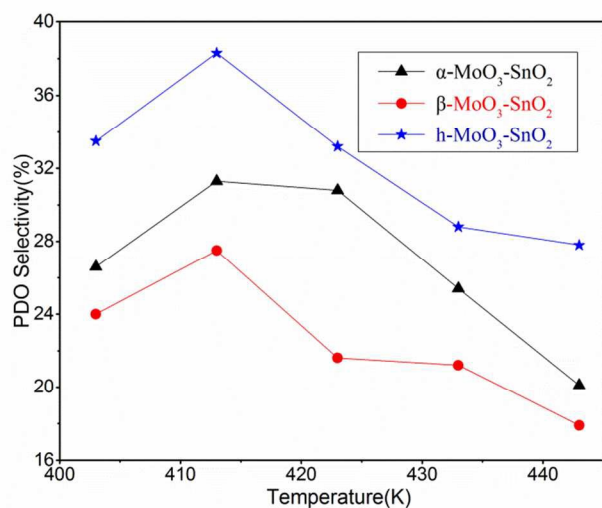
Fig.1 Effects of α-, β- and h-MoO$_3$-SnO$_2$ catalyst on PDO selectivity at different reaction temperature

these three catalysts, the selectivity of PDO increased initially and then decreased with the increasing reaction temperature. As a result of this trend, the highest selectivity of PDO over α-, β- and h-MoO$_3$-SnO$_2$ catalyst could reach 31.3%, 27.5% and 38.3% at 413 K, respectively, which can be attributed to the appropriate cooperation of acid sites, base sites and redox sites under this condition. The acid sites and redox sites have a great effect on the cleavage of C-O bond, the acid sites and base sites have a great effect on the cleavage of C-H bond and association of C-C bond, and these effects would be disused in the characterization part.
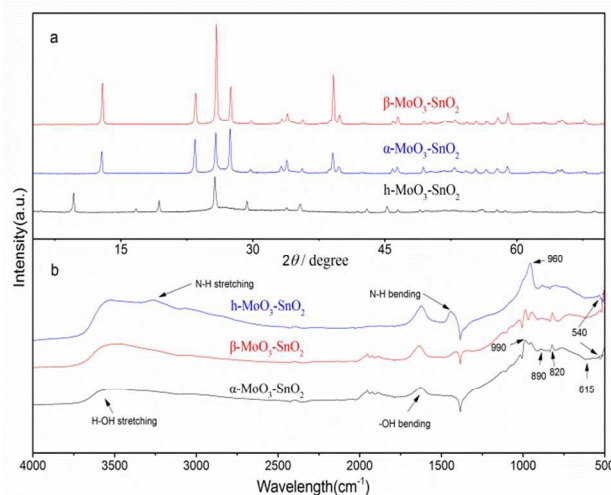
Fig.2 XRD profile (a) and IR spectra (b) of α-, β- and h-MoO$_3$-SnO$_2$ catalyst

With the increasing reaction temperature, the selectivity of CH$_3$OH increased constantly over α- and β-MoO$_3$-SnO$_2$ catalysts while decreased constantly over h-MoO$_3$-SnO$_2$ catalyst. The selectivity of FA decreased constantly over β-MoO$_3$-SnO$_2$ catalyst while increased constantly over h-MoO$_3$-SnO$_2$ catalyst. The selectivity of MF decreased initially then increased over α-MoO$_3$-SnO$_2$ catalyst while increased firstly then decreased over h-MoO$_3$-SnO$_2$ catalyst. As presented in Fig.1, the highest selectivity of PDO was always obtained over h-MoO$_3$-SnO$_2$ catalyst and the lowest selectivity of PDO was always obtained over β-MoO$_3$-SnO$_2$ catalyst at a certain reaction temperature, therefore, characterizations related to MoO$_3$ bulk structure, the interaction between SnO$_2$ and MoO$_3$, surface property and the morphology and microstructure were carried out in detail to investigate the reasons concerning the phenomenon in Fig.1.

3.2 XRD profiles and IR spectra

Fig.2 shows XRD profiles and IR spectra of α-, β- and h-MoO$_3$-SnO$_2$ catalysts. As exhibited in Fig.2a, the peaks at 12.8 °, 23.3 °, 25.7 °, 27.3 °, 33.8 °, 39.7 °are assigned to orthorhombic[22] MoO$_3$ (α) (PDF card NO.35-0609), the peaks at 12.8 °, 23.7 °, 25.8 °, 27.3 °, 33.7 °, 39.2 °are assigned to monoclinic MoO$_3$ (β) (PDF card NO.47-1320), the peaks at 9.7 °,16.7 °, 19.5 °, 25.8 °, 29.4 °, 35.5 ° are assigned to hexagonal MoO$_3$ (h) (PDF card NO.21-0569). Obviously, the bulk structure of α-MoO$_3$ is similar with that of β-MoO$_3$ while markedly different from that of h-MoO$_3$. The broadening peaks at 26.6 °, 33.9 °, 37.9 °, 51.7 °are assigned to tetragonal SnO$_2$ (PDF card NO.41-1445), however, the intensity of broadening peaks is completely weak compared to that of MoO$_3$, this notable scrutiny can be explained either due to incorporation of MoO$_3$ into SnO$_2$ lattice or the amorphous nature of the SnO$_2$. In Fig.2b, the peak at 540 cm^{-1} is associated with the Mo$_3$-O stretching vibration, which results from the edge-shared oxygen in common with three MoO$_6$ octahedra[23]. The peaks at 540 cm^{-1} of β- MoO$_3$-SnO$_2$ catalyst do not occur while that of α- and h-MoO$_3$-SnO$_2$ catalyst clearly occur, which is consistent with the bulk structure of edge-shared oxygen existing in α- and h-MoO$_3$-SnO$_2$ catalysts while not existing in β- MoO$_3$-SnO$_2$ catalyst. The peaks at 820

This journal is © The Royal Society of Chemistry [2015]

Catal. Sci. Technol., [2015], **[vol]**, 00–00 | 3

Table 2 Textural properties of α-, β- and h-MoO₃-SnO₂ catalysts

Cat	S^a_{BET} (m²/g)	V^b_{micro} (cm³/g)	Pore size (nm)
α	7.77	0.00043	12.82
β	22.46	0.00027	12.51
h	8.10	0.00110	9.85

[a] determined by t-method; [b] determined by BJH-method.

cm⁻¹ and 890 cm⁻¹ are attributed to the Mo-O-Mo vibration of Mo⁺⁶ as a consequence of two MoO₆ octahedra having a corner-shared oxygen in common[24], the peaks at 820 and 960 cm⁻¹ of h-MoO₃-SnO₂ catalyst are apparently broadening compared to α- and β-MoO₃-SnO₂ catalysts, indicating the weak interaction between MoO₃ and SnO₂ consistent with the results of XPS in Fig.3, which makes SnO₂ and MoO₃ disperse more homogeneously. The peaks at 990 cm⁻¹ are ascribed to Mo=O stretching vibration[25], which is a basic characteristic of layered MoO₃ phase. The Mo=O stretching vibration of h-MoO₃-SnO₂ catalyst is shifted to 960 cm⁻¹ compared to that of the other two catalysts, suggesting more hydrated surface of h-MoO₃-SnO₂ catalyst exists and indicating stronger Bronsted acidity than that of the other two catalysts, which was constituent with the results of Fig.4b. The peaks at 615 cm⁻¹ are due to Sn-O stretching vibration[26], there are not apparent differences between them. Hexagonal MoO₃ is dispersed more homogeneously over h-MoO₃-SnO₂ catalyst due to the weak interaction between MoO₃ and SnO₂ and the hexagonal crystalline tunnel structure existing in h-MoO₃-SnO₂ catalyst, besides, more hydrated surface of h-MoO₃-SnO₂ catalyst can lead to more Bronsted acidity on the catalyst surface, which is beneficial for the dissociation of C-O bond in DMET and the reaction of DMET to PDO.

3.3 Surface texture properties.

The surface texture properties obtained for α-, β- and h-MoO₃-SnO₂ catalysts are listed in Table 2. The micropore volume exhibited by h-MoO₃-SnO₂ catalyst is extremely larger than that of the other two catalysts, which is ascribed to the hexagonal crystalline tunnel structure[27] existing in h-MoO₃-SnO₂ catalyst. The bigger micropore volume shown in Table 2 and decreasing interaction between MoO₃ and SnO₂ verified in Table 3 make MoO₃ disperse more homogeneously over SnO₂ surface and provide enough space for the catalytic oxidation of DMET to PDO. The BET surface exhibited by β-MoO₃-SnO₂ catalyst is extremely larger than that of the other two catalysts, which is due to the lattice distortions induced by the substitution of Mo⁶⁺ ions into the tin oxide lattice[28]. It has been reported that an excess negative charge induced by non-equivalent M₁-O-M₂ bonds can lead to stronger acidic properties by dissociation absorbed water, which is consistent with results of NH₃-TPD in Fig.4. The bigger micropore volume of h-MoO₃-SnO₂ catalyst is good for the reaction of DMET to PDO while stronger acidity and stronger oxidation ability of β-MoO₃-SnO₂ catalyst are in favour of bypass reaction of DMET to FA and MF.

3.4 XPS

Fig.3 depicts Sn 3d core level, Mo 3d core level and O 1s core level XP spectra of α-, β- and h-MoO₃-SnO₂ catalysts, respectively. In Fig.3, the peaks with a spin–orbit doublet at 232.9 eV and 236.2 eV correspond to the presence of Mo⁶⁺ oxidation state[29], the peaks with a spin-orbit doublet at 486.8 eV

Table 3 XPS data of α-, β- and h-MoO₃-SnO₂ catalysts

Cat	O 1s	Sn 3d₅/₂	Mo 3d₅/₂	ΔBE$_{O-Sn}$	ΔBE$_{O-Mo}$
h	531.0	487.1	233.1	43.9	297.9
α	530.7	486.9	232.9	43.8	297.8
β	529.4	485.8	231.8	43.6	297.6
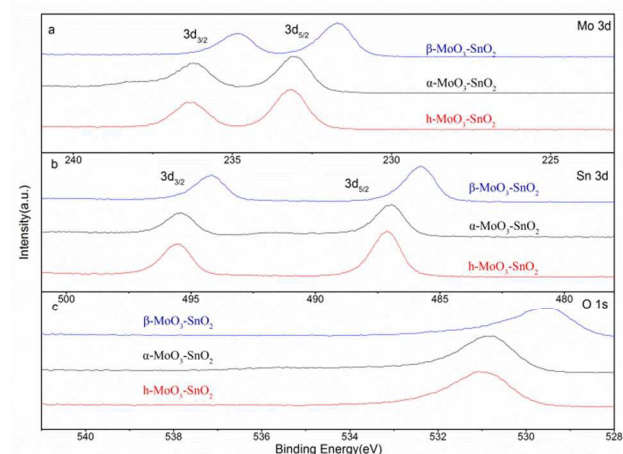
Fig. 3 Mo 3d (a), Sn 3d (b) and O 1s (c) XP spectra of α-, β- and h-MoO₃-SnO₂ catalysts

and 495.5 eV confirm the presence of Sn⁴⁺ oxidation state[28], the peak at about 530.8 eV indicates the presence of oxygen species[26]. The binding energies of Mo 3d, Sn 3d and O 1s were significantly increased from β-MoO₃-SnO₂ catalyst to h-MoO₃-SnO₂ catalyst, respectively, indicating the decreasing electronic density in Mo-O bond and Sn-O bond, and the binding energy displacements of Mo 3d, Sn 3d and O 1s suggest the incorporation of molybdenum into the SnO₂ lattice, which is induced by the transformation of MoO₃ morphology. In Table 3, the estimated binding energy (ΔBE) differences between the O 1s and Sn 3d₅/₂ core levels and the difference between the O 1s and Mo 3d₅/₂ core levels are significantly increased from β-MoO₃-SnO₂ catalyst to h-MoO₃-SnO₂ catalyst. This remarkable observation can be ascribed to the reduction of the interatomic spacing upon the substitution of Sn⁴⁺ ion (0.71Å)[28] with smaller sized Mo⁶⁺ ion (0.62Å) and consequently contraction of the SnO₂ lattice strengthens the oxygen vacancies in β-MoO₃-SnO₂ catalyst, which is consistent with results of Raman in Fig.5. Therefore, the lattice strain and oxygen vacancies in β-MoO₃-SnO₂ catalyst induced by the substitution of Sn⁴⁺ ion with smaller sized Mo⁶⁺ ion enhance the oxidation ability of β-MoO₃-SnO₂ catalyst so that more CH₃O· can be formed and consequently transformed to FA and MF, which is consistent with the results in Table 1 that the total FA and MF selectivity was always highest while the selectivity of PDO selectivity was always lowest obtained over β-MoO₃-SnO₂ catalyst at the same time. The moderate oxidation ability of h-MoO₃-SnO₂ catalyst which can be concluded from the Table 3 and Fig.5 is appropriate for the dissociation of C-H bond in DMET with the assistance of basicity as respect to the highest PDO selectivity obtained over h-MoO₃-SnO₂ catalyst.

3.4 NH₃-TPD and NH₃-IR

NH₃-TPD and NH₃-IR profiles of α-, β- and h-MoO₃-SnO₂ catalysts are presented in Fig.4, respectively. In Fig.4a, there exist

4 | *Catal. Sci. Technol.*, [2015], **[vol]**, 00–00

This journal is © The Royal Society of Chemistry [2015]
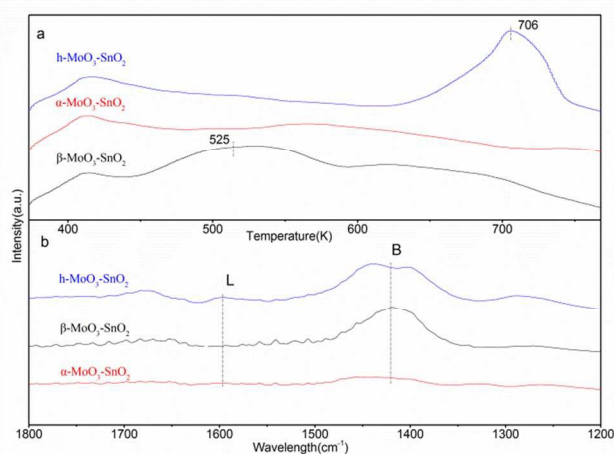
Fig.4 NH$_3$-TPD (a) and NH$_3$-IR (b) profiles of α-, β- and h-MoO$_3$-SnO$_2$ catalyst
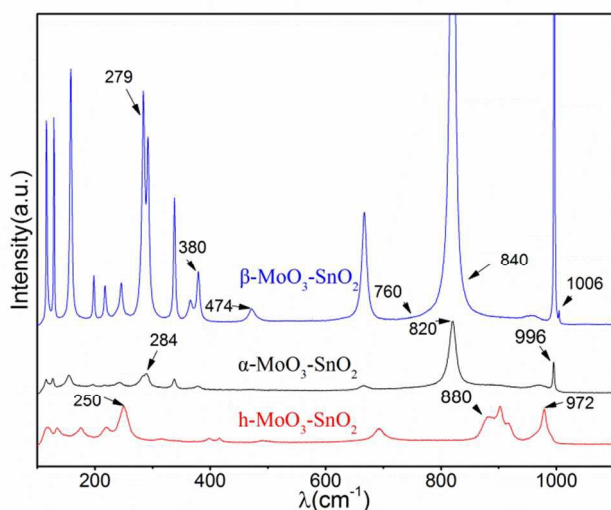
Fig.5 Raman spectra of α-, β- and h-MoO$_3$-SnO$_2$ catalysts

two NH$_3$ desorption peaks over all of these three catalysts, the weak acid peaks are almost same, however, the strong acid peaks are distinctively different. The strong acid peak of h-MoO$_3$-SnO$_2$ catalyst is shifted to the higher temperature of 706 K compared to the temperature of 525 K over β-MoO$_3$-SnO$_2$ catalyst, besides, the number of strong acid sites of h-MoO$_3$-SnO$_2$ catalyst is apparently more than that of β-MoO$_3$-SnO$_2$ catalyst, and this observation can be ascribed to the residual NH$_4^+$ existing in the h-MoO$_3$-SnO$_2$ catalyst[25] which is consistent with the result of IR in Fig.2. In Fig.4b, the peak at 1420 cm^{-1} is assigned to Brønsted acid and 1605 cm^{-1} is assigned to the Lewis acid [3], h-MoO$_3$-SnO$_2$ catalyst exhibits most Brønsted acid sites and Lewis acid sites, besides, β-MoO$_3$-SnO$_2$ catalyst also has more Brønsted acid sites than that of α-MoO$_3$-SnO$_2$ catalyst. Mo[30] ions in the catalysts have been reported to provide the Brønsted acid sites. The most acid sites existing on the surface of h-MoO$_3$-SnO$_2$ catalyst can provide enough acid sites to dissociate C-O bond in DMET molecule and make the C-C bond coupled together with the assistance of moderate oxidation sites, which is good for the highest PDO selectivity obtained over h-MoO$_3$-SnO$_2$ catalyst.

3.5 Raman

Fig.5 shows the Raman spectra of α-, β- and h-MoO$_3$-SnO$_2$ catalysts. The peaks at 279, 760, 840 cm^{-1} are characteristic[31] of β-MoO$_3$, the peaks at 284, 820, 996 cm^{-1} are characteristic[32] of α-MoO$_3$, and the peaks at 250, 890, 972 cm^{-1} are characteristic of h-MoO$_3$ .The peak intensity of β-MoO$_3$-SnO$_2$ catalyst at 474 cm^{-1} assigned to the vibration of oxygen[28] is obviously stronger than that of the other two catalysts, which is consistent with the results of XPS in Fig.3 and BET in Table 2, the stronger vibration of oxygen is in favour of the formation of oxygen vacancies and makes the catalyst possess stronger oxidation ability, the peak of β-MoO$_3$-SnO$_2$ catalyst at 380, 1006 cm^{-1} assigned[33] to SnMoO$_4$ indicates the presence of tetrahedral molybdenum oxide. The stronger oxidation ability of β-MoO$_3$-SnO$_2$ catalyst with appropriate acid sites is in favour of the formation of FA and subsequent formation of MF, which explains why the total selectivity of FA and MF over β-MoO$_3$-SnO$_2$ catalyst is higher than that of the other two catalysts in Table 1. The peak position of h-MoO$_3$-SnO$_2$ catalysts at 972 cm^{-1} corresponding to Mo=O vibration is shifted to lower wavenumber position compared to that of the other two catalysts, which can be ascribed to the hydrated condition[34] of the catalyst surface. More -OH groups of the hydrated catalyst surface and bigger micropore volume of h-MoO$_3$-SnO$_2$ catalyst tend to absorb DMET and provide more reaction space, the stronger Bronsted acitity can dissociate C-O bond of DMET more easily and the moderate oxidation ability of h-MoO$_3$-SnO$_2$ catalyst is good for C-H dissociation and C-C association, which leads to the highest PDO selectivity over h-MoO$_3$-SnO$_2$ catalyst and lowest PDO selectivity over β-MoO$_3$-SnO$_2$ catalyst.

3.6 TEM and SEM

TEM images of α-, β- and h-MoO$_3$-SnO$_2$ catalysts are shown in Fig.6 and Fig.S1-S3. The lattice fringe spacing of MoO$_3$ is observed to be 0.37 nm, 0.34 nm and 0.35 nm, corresponding to the atomic spacing of (001)[22, 35] in α-MoO$_3$, (002) in β-MoO$_3$ and (210) in h-MoO$_3$ respectively. The conclusion can be drawn that all these three kinds of MoO$_3$ were dispersed on the surface of SnO$_2$ based on TEM images. SEM images of α-, β- and h-MoO$_3$-SnO$_2$ catalysts are shown in Fig.7 and Fig.S4-S6. The particle diameter of α- and h-MoO$_3$-SnO$_2$ is smaller than that of β-MoO$_3$-SnO$_2$; therefore it indirectly indicates that the stronger interaction between MoO$_3$ and SnO$_2$ exists in β-MoO$_3$-SnO$_2$ compared to α- and h-MoO$_3$-SnO$_2$, which is consistent with the results of XPS.

Based on the conclusions drawn from the images of TEM and SEM, a proper model of MoO$_3$-SnO$_2$ is proposed in Scheme 1. In the model of MoO$_3$-SnO$_2$, all these three kinds of MoO$_3$ were dispersed on the surface of SnO$_2$. Besides, a possible reaction pathway from DMET to PDO over MoO$_3$-SnO$_2$ catalyst is also shown in Scheme 1. The molecule of DMET was initially adsorbed on the surface of MoO$_3$-SnO$_2$ catalyst; then the C-O bond was dissociated over the acid sites provided by Mo[36] ions, C-H bond was dissociated and C-C bond was connected over base sites[8, 21, 37] with the assistance of the redox sites at the same time, the product of DMET was then formed and desorbed from the surface of MoO$_3$-SnO$_2$ catalyst. The acid sites, base sites and redox sites all have played important roles in the reaction from DMET to PDO, however, the acid sites are possibly more important than the base sites and redox sites. More hydrated surface of h-MoO$_3$-SnO$_2$ catalyst can lead to more Bronsted acid

This journal is © The Royal Society of Chemistry [2015]

Catal. Sci. Technol., [2015], **[vol]**, 00–00 | 5
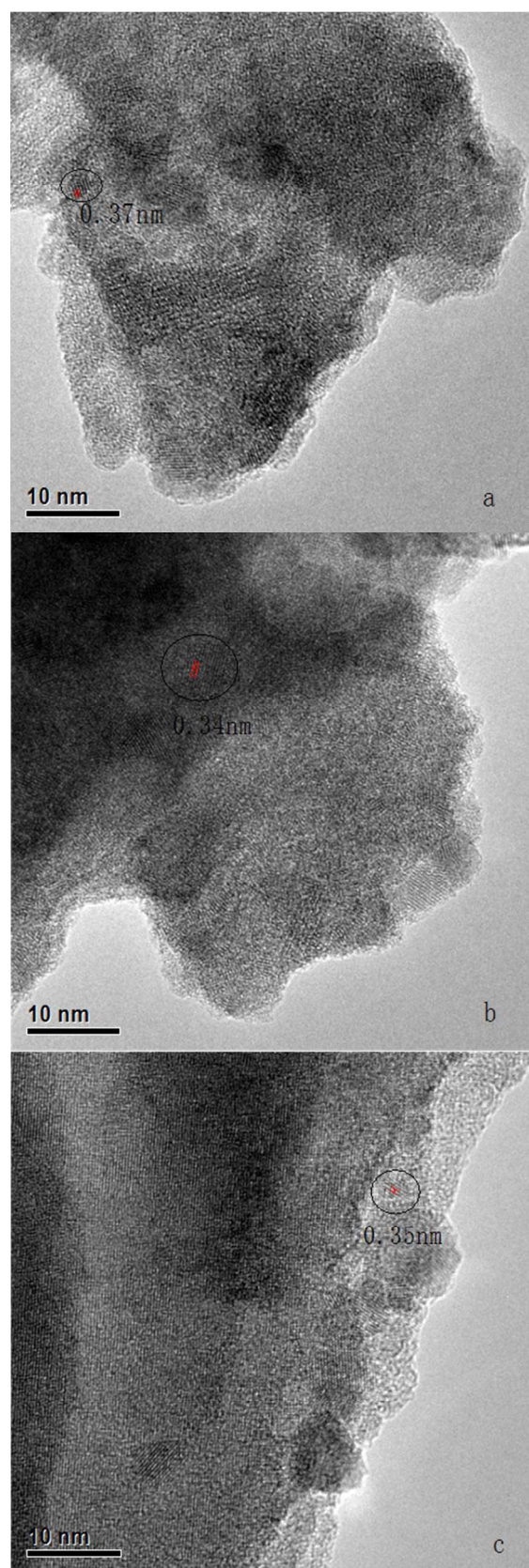
Fig. 6 TEM images of α-MoO$_3$-SnO$_2$ (a), β-MoO$_3$-SnO$_2$ (b) and h-MoO$_3$-SnO$_2$ (c) catalysts

sites on the catalyst surface and favor the dissociation of C-O
5 bond in DMET, which has a positive connection with the high
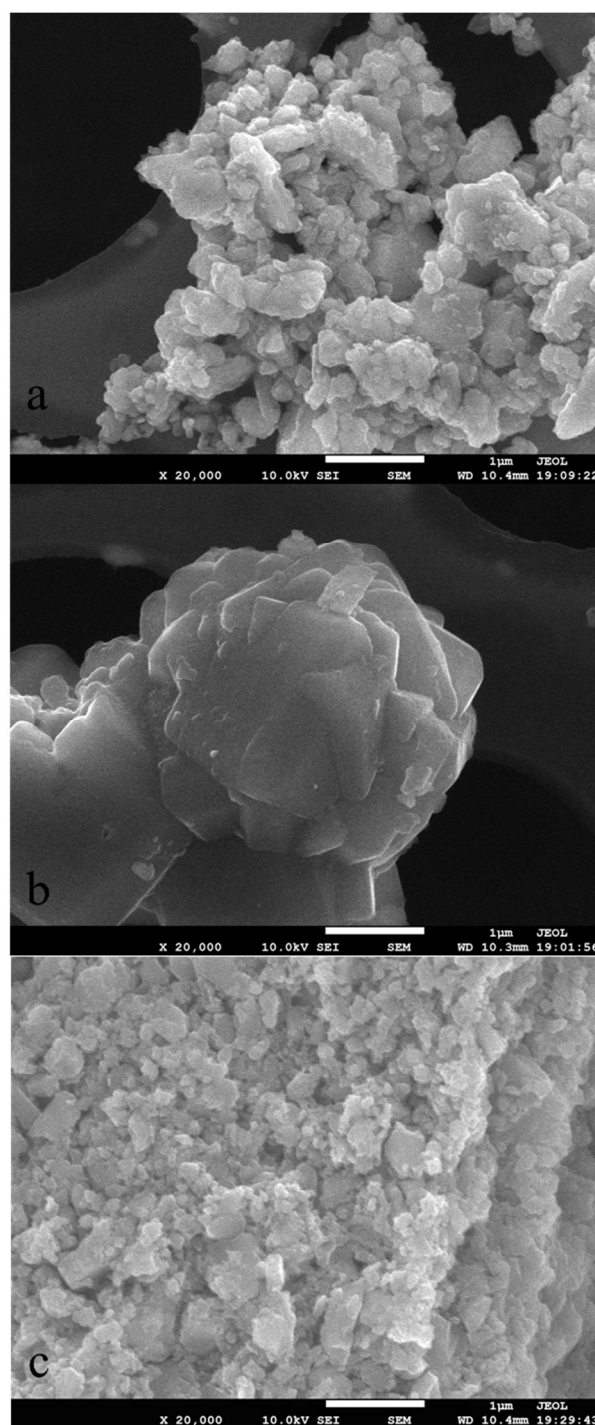
Fig. 7 SEM images of α-MoO$_3$-SnO$_2$ (a), β-MoO$_3$-SnO$_2$ (b) and h-MoO$_3$-SnO$_2$ (c) catalysts

selectivity of PDO obtained over h-MoO$_3$-SnO$_2$ catalyst.

10   With the increasing reaction temperature, the highest
selectivity of PDO was always obtained over h-MoO$_3$-SnO$_2$
catalyst and the lowest selectivity of PDO was always obtained
over β-MoO$_3$-SnO$_2$ catalyst. As exhibited in Table 2, the
hexagonal crystalline tunnel structure existing in h-MoO$_3$ makes
15 h-MoO$_3$-SnO$_2$ catalyst have much bigger micropore volume than
that of α- and β-MoO$_3$-SnO$_2$ catalysts, which provides enough
reaction space for the reaction of DMET to PDO. In Fig.2, the
bulk structure of β-MoO$_3$-SnO$_2$ catalyst is similar with that of

6 | *Catal. Sci. Technol.*, [2015], **[vol]**, 00–00

This journal is © The Royal Society of Chemistry [2015]
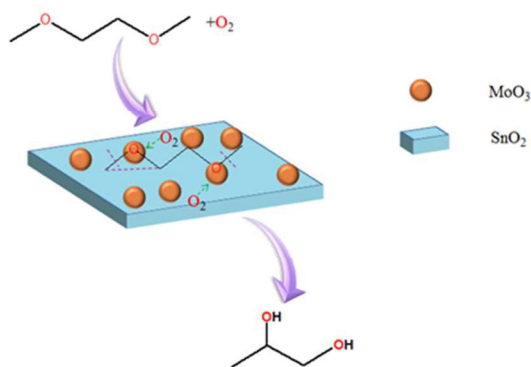
Scheme 1 Schematic illustration of possible reaction pathway from DMET to PDO

α-MoO$_3$-SnO$_2$ catalyst while markedly different from that of h-MoO$_3$-SnO$_2$ catalyst. The intensity of broadening peaks corresponding to SnO$_2$ is completely weak compared to that of MoO$_3$, which can be ascribed to incorporation of molybdnuem into the SnO$_2$ lattice. Because of the weak interaction between MoO$_3$ and SnO$_2$ and the hexagonal crystalline tunnel structure existing in h-MoO$_3$-SnO$_2$ catalyst, hexagonal MoO$_3$ is dispersed more homogeneously over h-MoO$_3$-SnO$_2$ catalyst, besides, more hydrated surface of h-MoO$_3$-SnO$_2$ catalyst can lead to more Bronsted acid sites on the catalyst surface, which is in favour of the dissociation of C-O bond in DMET and association of C-C bond with assistance of moderate redox sites and base sites. The binding energy of Mo 3d, Sn 3d and O 1s in Fig.3 is increased significantly from β-MoO$_3$-SnO$_2$ catalyst to h-MoO$_3$-SnO$_2$ catalyst, respectively, indicating the decreasing electronic density in Mo-O bond and Sn-O bond, and the binding energy displacements of Mo 3d, Sn 3d and O 1s suggest the incorporation of molybdenum into the SnO$_2$ lattice, which is induced by the transformation of MoO$_3$ morphology. In Table 3, ΔBE_{O-Sn} and ΔBE_{O-Mo} are significantly reduced from h-MoO$_3$-SnO$_2$ catalyst to β-MoO$_3$-SnO$_2$ catalyst, suggesting the electronic interaction between Sn and Mo is increased. The stronger lattice strain and more oxygen vacancies in β-MoO$_3$-SnO$_2$ catalyst induced by the substitution of Sn^{4+} ion with smaller sized Mo^{6+} ion enhance the oxidation ability of β-MoO$_3$-SnO$_2$ catalyst so that more CH$_3$O· can be formed and consequently transformed to FA and MF, which is consistent with the results in Table 1 that the total FA and MF selectivity was always highest obtained over β-MoO$_3$-SnO$_2$ catalyst while the lowest PDO selectivity was obtained at the same time. The acid sites on the surface of h-MoO$_3$-SnO$_2$ catalyst can provide enough acid sites to dissociate C-O bond in DMET molecule and associate C-C bond to produce PDO with assistance of moderate redox sites induced by oxygen vacancies which can be verified by Raman results in Fig.5. Therefore, characterizations related to bulk structure, the interaction between MoO$_3$ and SnO$_2$, surface property and the morphology and microstructure of these three catalysts can account for why the selectivity of PDO was highest over h-MoO$_3$-SnO$_2$ catalyst and lowest over β-MoO$_3$-SnO$_2$ catalyst.

Conclusions

Because of the weak interaction between MoO$_3$ and SnO$_2$ and the hexagonal crystalline tunnel structure existing in h-MoO$_3$-SnO$_2$ catalyst, hexagonal MoO$_3$ is dispersed more homogeneously over h-MoO$_3$-SnO$_2$ catalyst, besides, more hydrated surface of h-MoO$_3$-SnO$_2$ catalyst can lead to more Bronsted acid sites on the catalyst surface. The lattice strain and oxygen vacancies in β-MoO$_3$-SnO$_2$ catalyst induced by the substitution of Sn^{4+} ion with smaller sized Mo^{6+} ion enhance the oxidation ability of β-MoO$_3$-SnO$_2$ catalyst, consequently more CH$_3$O· can be formed and transformed to FA and MF. These findings explain why the highest selectivity of PDO was always obtained over h-MoO$_3$-SnO$_2$ catalyst and the lowest selectivity of PDO was always obtained over β-MoO$_3$-SnO$_2$ catalyst with the increasing reaction temperature and these promising results are pretty significant for further investigation of rational design of MoO$_3$-SnO$_2$ catalyst structure applied for the reaction of DMET to PDO.

Notes and references

^{a} *State Key Laboratory of Coal Conversion, Institute of Coal Chemistry, Chinese Academy of Sciences, Taiyuan 030001, China;*
^{b} *University of Chinese Academy of Sciences, Beijing 100049, China.*
^{c} *Department of Applied Chemistry, School of Engineering, University of Toyama, Gofuku 3190, Toyama 930-8555, Japan*
†*Electronic Supplementary Information (ESI) available: [details of any supplementary information available should be included here]. See DOI: 10.1039/b000000x/*
‡ mail: tan@sxicc.ac.cn. Tel:+86-351-4044287. Fax:+86-351-4044287.
  qdzhang@sxicc.ac.cn.Tel:+86-351-4044287.Fax:+86-351-4044287.

1. H. C. Liu, P. Cheung and E. Iglesia, *J Catal*, 2003, 217, 222-232.
2. H. C. Liu and E. Iglesia, *J Catal*, 2002, 208, 1-5.
3. G. B. Liu, Q. D. Zhang, Y. Z. Han, N. Tsubaki and Y. S. Tan, *Green Chem*, 2013, 15, 1501-1504.
4. G. B. Liu, Q. D. Zhang, Y. Z. Han, N. Tsubaki and Y. S. Tan, *Green Chem*, 2015, 17, 1057-1064.
5. G. Liu, Q. Zhang, Y. Han and Y. Tan, *Cata Commun*, 2012, 26, 173-177.
6. Q. Zhang, Y. Tan, C. Yang and Y. Han, *J Mol Catal A*, 2007, 263, 149-155.
7. Q. Zhang , Y. Tan , G. Liu, J. Zhang and Y. Han, *Green Chem*, 2014, 11, 4708-4715.
8. H. Yagita, K. Asami, A. Muramatsu and K. Fujimoto, *Applied Catal*, 1989, 53, 5-9.
9. Z. L. Yuan, P. Wu, J. Gao, X. Y. Lu, Z. Y. Hou and X. M. Zheng, *Catal Lett*, 2009, 130, 261-265.
10. D. Tongsakul, S. Nishimura and K. Ebitani, *J Phys Chem C*, 2014, 118, 11723-11730.
11. M. Niculescu, I. Ledeti and M. Birzesc, *J Organomet Chem*, 2014, 767, 108-111.
12. G. M. Peng, X. C. Wang, X. F. Chen, Y. J. Jiang and X. D. Mu, *J Ind Eng Chem*, 2014, 20, 2641-2645.
13. D. L. Sun, R. Narita, F. Sato, Y. Yamada and S. Sato, *Chem Lett*, 2014, 43, 450-452.
14. C. D'Agostino, Y. Ryabenkova, P. J. Miedziak, S. H. Taylor, G. J. Hutchings, L. F. Gladden and M. D. Mantle, *Catal Sci Technol*, 2014, 4, 1313-1322.
15. Z. W. Huang, J. Chen, Y. Q. Jia, H. L. Liu, C. G. Xia and H. C. Liu, *Applied Catal B*, 2014, 147, 377-386.
16. S. X. Xia, R. F. Nie, X. Y. Lu, L. N. Wang, P. Chen and Z. Y. Hou, *J Catal*, 2012, 296, 1-11.

17. S. X. Xia, W. C. Du, L. P. Zheng, P. Chen and Z. Y. Hou, *Catal Sci Technol*, 2014, 4, 912-916.
18. Z. W. Huang, F. Cui, H. X. Kang, J. Chen, X. Z. Zhang and C. G. Xia, *Chem Mater*, 2008, 20, 5090-5099.
19. Z. W. Huang, F. Cui, J. J. Xue, J. L. Zuo, J. Chen and C. G. Xia, *Catal Today*, 2012, 183, 42-51.
20. Y. Liu, C. Luo and H. C. Liu, *Angew Chem Int Ed*, 2012, 51, 3249-3253.
21. S. Arndt, T. Otremba, U. Simon, M. Yildiz, H. Schubert and R. Schomäcker, *Applied Catal A*, 2012, 425-426, 53-61.
22. L. L. Xing, S. A. Yuan, Z. H. Chen, Y. J. Chen and X. Y. Xue, *Nanotechnology*, 2011, 22, 6.
23. T. H. Chiang and H. C. Yeh, *Materials*, 2013, 6, 4609-4625.
24. L. Q. Mai, B. Hu, W. Chen, Y. Y. Qi, C. S. Lao, R. S. Yang, Y. Dai and Z. L. Wang, *Adv Mater*, 2007, 19, 3712-3716.
25. A. Chithambararaj, N. S. Sanjini, A. C. Bose and S. Velmathi, *Catal Sci Technol*, 2013, 3, 1405-1414.
26. M. Martos, J. Morales and L. Sanchez, *J Mater Chem*, 2002, 12, 2979-2984.
27. J. N. Guo, Y. Zhao, J. Z. Zhao, J. J. Wu, Y. H. Song, Y. X. Tan, F. P. Wang, X. L. Hao, Y. Lu and F. X. Bao, *Eur J Inorg Chem*, 2014, 21, 3322-3329.
28. B. Mallesham, P. Sudarsanam, G. Raju and B. M. Reddy, *Green Chem*, 2013, 15, 478-489.
29. L. X. Song, J. Xia, Z. Dang, J. Yang, L. B. Wang and J. Chen, *Crystengcomm*, 2012, 14, 2675-2682.
30. M. Niwa and J. Igarashi, *Catalysis Today*, 1999, 52, 71-81.
31. I. E. Wachs, *Catal Today*, 1996, 27, 437-455.
32. M. A. Banares, H. C. Hu and I. E. Wachs, *J Catal*, 1994, 150, 407-420.
33. D. S. Zingg, L. E. Makovsky, R. E. Tischer, F. R. Brown and D. M. Hercules, *J Phys Chem*, 1980, 84, 2898-2906.
34. P. E., K. S., G. J. and B. J. P., *J Raman Spectrosc*, 1986, 17, 233-241.
35. X. Y. Xue, Z.-H. Chen, L. L. Xing, S. Yuan and Y. J. Chen, *Chem Commun*, 2011, 47, 5205-5207.
36. V. Lochar, *Applied Catal A*, 2006, 309, 33-36.
37. S. Pak, P. Qiu and J. H. Lunsford, *J Catal*, 1998, 179, 222-230.